

Numerical Simulations of Complex Nonsymmetrical 3D Systems for Scanning Electrochemical Microscopy Using the Boundary Element Method

Oleg Sklyar[†] and Gunther Wittstock*

Department of Chemistry (FB9) and Institute of Chemistry and Biology of the Marine Environment (ICBM),
Carl von Ossietzky University of Oldenburg, D-26111 Oldenburg, Germany

Received: January 31, 2002; In Final Form: May 13, 2002

Quantitative treatment of the problems related to scanning electrochemical microscopy (SECM) is performed by means of numerical simulations using the boundary element method (BEM). The method is used to calculate the amperometric steady-state response of a microelectrode or nanoelectrode of a given arbitrary geometry in the SECM feedback mode above surfaces with ideal negative feedback or diffusion-controlled positive feedback. By changing the problem setup from the interior to the exterior Laplace formalism, the precision of the calculation could be improved significantly because the exterior formulation does not require any assumptions about the extension of the diffusion layer at infinite time. The improved precision was demonstrated by simulations of standard problems that have been treated before by finite difference methods. Subsequently a series of simulations is presented that explores the effects of deviations from idealized SECM geometries used in many available finite difference simulations. Such deviations from ideal geometries are frequently encountered in routine SECM experiments and exert a varying influence on the precision of the obtained data and derived physicochemical parameters. Because of the speed of calculation and the flexibility of the geometric arrangements, entire SECM line scans were simulated and used to analyze some issues of recently introduced SECM instruments with integrated distance control mechanisms.

I. Introduction

Over the past decade, scanning electrochemical microscopy (SECM) has become a powerful and established scanning probe technique to investigate interfacial reactions ranging from corrosion problems to biochemical reactions.^{1–15} In the SECM experiments, a Faradaic current, i_T , is measured at the ultramicroelectrode (UME) used as local probe.¹⁶ The current is controlled by diffusional flux of oxidizable/reducible particles from both the sample surface and the bulk solution toward the active area of the UME. In the SECM feedback mode, for which the presented simulations can be applied, a so-called mediator is added to the electrochemical cell. Usually one redox form of a quasireversible redox couple is added to the electrolyte as mediator. In this paper, it is assumed that the mediator is oxidized under diffusion-controlled conditions at the UME. The obtained conclusions can, of course, be adapted to SECM experiments where an appropriate mediator is reduced at the UME because only the reaction directions of the heterogeneous reactions at the UME and the sample need to be reversed. The concentration profile, and hence the diffusional fluxes and i_T , are greatly affected by a number of parameters: the UME-sample distance, d , the UME geometry (in case of microdisk electrodes often characterized by the ratio, RG , between the radius of the insulating sheath and the radius r_T of the active electrode area), the sample topography in the vicinity of the UME, and the reactivity of the sample in the vicinity of the UME.

The main merit of the technique is seen in the possibility to image the distribution of heterogeneous reaction rates. This is conceptually straightforward if ideally flat samples and perfectly symmetric UME can be applied. When investigating solid surfaces or biological tissues, this condition is usually not satisfied. Previous SECM applications with micrometer-sized UME could to some extent neglect the problem because the working distance (some radii of the UME, i.e., some micrometers) is often much larger than the roughness of the investigated surface. However, the problem has become evident very early when attempting to investigate practically relevant surfaces, and attempts to separate the influences of topography and local reactivity either experimentally^{17–19} or numerically²⁰ stem back to the beginning of the nineties. Currently, strong efforts are under way in many laboratories to decrease the size of the UMEs used as probes in order to increase the spatial resolution of SECM experiments in routine applications.^{21,22} When decreasing the UME size also d must be decreased. Therefore, topographic features on the sample become important that are negligible when working with micrometer-sized UMEs. Consequently, various protocols for current-independent UME-sample distance control are proposed for SECM devices. Besides shear force-based systems^{23,24} and impedance-based systems,²⁵ the SECM was hyphenated with scanning force microscopy (SFM)^{26–30} and electrochemical scanning tunneling microscopy (ECSTM)^{31,32} setups. All of these modifications aim to maintain a constant d during the electrochemical measurements by guiding the UME over the sample following the specimen topography. This reduces the effect of the sample topography on i_T . However, it will be shown below that it is principally impossible to eliminate the topographic influence completely. Furthermore, substantial difficulties are encountered when fabricating axisymmetric disc-shaped UMEs of submicrometer

* To whom correspondence should be addressed. Fax: (+49-441) 7983486. E-mail: gunther.wittstock@uni-oldenburg.de.

[†] Graduate Student at the Carl von Ossietzky University of Oldenburg and grantee of the Graduate Course GRK 152 "Physical Chemistry of the Surfaces and Interfaces" at the Wilhelm Ostwald Institute for Physical and Theoretical Chemistry at the University of Leipzig, Germany.

dimension. In many cases, increased spatial resolution is traded against a loss in control of the precise UME geometry and can give rise to artifacts in SECM images.

As pointed out by Mirkin et al.,^{21,33} the most informative characterization of SECM probes is obtained from i_T - d curves commonly referred to as approach curves. They are recorded by measuring the steady-state current in the SECM feedback mode while the UME is slowly approaching a flat sample of known reactivity. The curves are usually represented in normalized coordinates I vs L by plotting i_T in units of the UME current in quasi-infinite distance from the surface, $i_{T,\infty}$, versus d normalized by the radius of the UME, r_T . Under such conditions, the approach curve depends on the overall probe geometry. Experimental approach curves are usually compared to theoretical ones, obtained by numerical simulations in order to elucidate the geometry of the UME. Kwak and Bard³⁴ made first simulations of a microdisk electrode approach curves using the finite element method (FEM). Later on, FDM was used to simulate the influence of different experimental parameters on the SECM response.^{35–37} Recently, more refined calculations of microdisk UME were performed by Amphlett and Denuault³⁸ using the FDM with carefully adjusted grids highlighting the overall shape of the probe. The cases of conical, hemispherical, and ring probe geometries were also calculated by FDM.^{33,39,40} For the simplest case of a microdisk UME probe, there is also an analytical solution for the approach curves.⁴¹ Because of the difficulties in execution of FDM and FEM in three-dimensional (3D) space for complex geometries, all mentioned calculations deal with axisymmetric situations.

On the nanometer scale, manufacturing of ideal axisymmetric probes is difficult. The necessity in the analysis of the properties of such probes increases the need for their proper theoretical treatment. The lack of symmetry requires a three-dimensional representation of the simulation. Fulian et al.^{42–44} introduced the use of the boundary element method (BEM) for the numerical solution of the SECM problems. The same authors also gave a thorough explanation of the general advantages of the BEM compared to the FDM and FEM.⁴² In this paper, the possibility of solving pure 3D steady-state problems by BEM is used to describe the behavior of SECM probes that are nonsymmetric and to simulate line scans where the symmetry is broken by topographic features on the sample. The results allow to address issues of SECM resolution in the constant distance mode.

Hereafter, the problem formulation is changed from the interior Laplace formulation used by Fulian et al.^{42–44} to the exterior Laplace formulation in order to allow a more accurate treatment of the flux from the solution bulk to the UME. This decreases the computational errors significantly. The flux from the solution bulk governs $i_{T,\infty}$ in any case and $i_T(d)$ in case of the negligible sample reactivity. A number of SECM approach curves of axisymmetric electrodes were calculated as well to allow a comparison of the changed problem formulation with results obtained using FDM by Amphlett and Denuault³⁸ for microdisk UME probes, and by Selzer and Mandler³⁹ for hemispherical UME probes.

II. Theory

A. General Formulation. The detailed description of the BEM can be found elsewhere.^{45,46} In this contribution, only those issues are pointed out that are important either for a general understanding or those specific to the SECM simulations with the changed problem formulation. All calculations are made for the SECM feedback mode. Mediator oxidation at the UME is

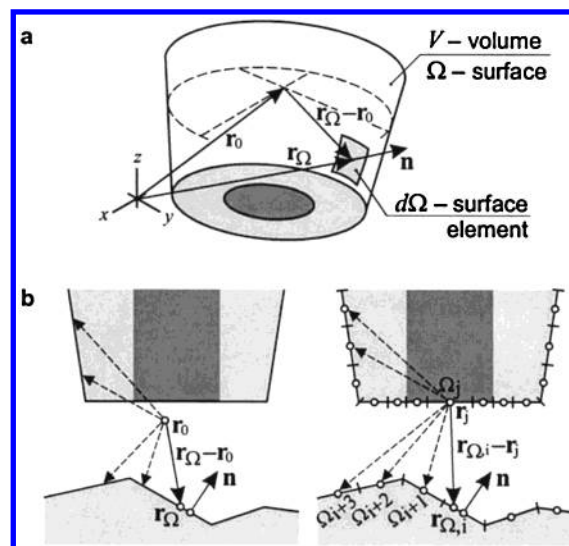


Figure 1. Notation for the analytical (a) and numerical (b) BEM formulations of SECM problems.

assumed:



where R stands for reduced species and O for oxidized and n is the number of electrons transferred per redox event. The mediator R is present in the solution bulk with a concentration c_R^* , whereas the bulk concentration of the oxidized mediator form O is zero ($c_O^* = 0$). Hereafter, the concentrations of R and O are normalized to the bulk concentration c_R^* of R and denoted as C_R and C_O , respectively. If i_T is diffusion-controlled, the mathematical description of the processes in the electrode vicinity is given by a set of diffusion equations containing partial derivatives of the concentrations C_R and C_O . Under the assumption of equality of the diffusion coefficients, D_R and D_O for both redox states

$$D_O = D_R = D \quad (2)$$

the mass conservation law can be invoked

$$C_R(\mathbf{r}, t) + C_O(\mathbf{r}, t) = 1 \quad (3)$$

where \mathbf{r} denotes the vector of three generalized space coordinates. Taking into consideration eqs 2 and 3, the system can be reduced to only one equation. For reasons of convenience the following variable substitutions are used below

$$\begin{aligned} C(\mathbf{r}, t) &= C_O(\mathbf{r}, t) \\ C_R(\mathbf{r}, t) &= 1 - C(\mathbf{r}, t) \end{aligned} \quad (4)$$

Thus, the diffusion equation in partial derivatives governing the mediator system assumes the following form:

$$\frac{\partial C(\mathbf{r}, t)}{\partial t} = D \cdot \nabla^2 C(\mathbf{r}, t), (\mathbf{r} \in V) \quad (5)$$

where V is the volume, for which the equation holds, and

$$\nabla^2 C(\mathbf{r} = (x, y, z), t) = \frac{\partial^2 C}{\partial x^2} + \frac{\partial^2 C}{\partial y^2} + \frac{\partial^2 C}{\partial z^2} \quad (6)$$

defines the Laplace operator in Cartesian coordinates. Additional notations are given in Figure 1a. The boundary surface of the

simulation space is indicated by Ω . Correspondingly, the vector \mathbf{r}_0 denotes the coordinates of an arbitrary point within the simulation domain for which the solution is to be found, and \mathbf{r}_Ω stands for the coordinates of a point at the boundary of the simulation space. Vector \mathbf{n} with length unity describes the direction of the outward surface normal for a surface element $d\Omega$ of the boundary.

Unlike the FEM and FDM, that directly solve eq 5 numerically, the BEM uses an integral equivalent of eq 5 that is defined as a surface integral over the boundary of the simulation domain ($\oint_{\Omega} f$). Although it is possible in principle to apply the BEM directly for the solution of transient problems,⁴⁷ this contribution deals with the steady-state situations. Because of the small dimensions of the UME in the micrometer or even nanometer size regime, the steady state is attained within some seconds or even less. Thus, the experimental measurements are usually performed under steady-state conditions, and $i_T(d)$ does not depend on time. Mathematically, this means eq 5 turns into the Laplace equation

$$\frac{\partial C(\mathbf{r}, t)}{\partial t} = 0 = \nabla^2 C(\mathbf{r}, t), (\mathbf{r} \in V) \quad (7)$$

The integral equivalent of eq 7 for the use in the BEM is derived with the help of the Green's second theorem and the Green's function, $G(\mathbf{r}_\Omega, \mathbf{r}_0)$.^{45,46}

$$C(\mathbf{r}_0) = \oint_{\Omega} \left(C(\mathbf{r}_\Omega) \frac{\partial G(\mathbf{r}_\Omega, \mathbf{r}_0)}{\partial \mathbf{n}} - G(\mathbf{r}_\Omega, \mathbf{r}_0) \frac{\partial C(\mathbf{r}_\Omega)}{\partial \mathbf{n}} \right) d\Omega, \quad (\mathbf{r}_0 \in V, \mathbf{r}_\Omega \in \Omega) \quad (8)$$

A symbolic representation is given in Figure 1b, left. The Green's function does not depend on the system geometry but on its dimensionality. The three-dimensional Green's function⁴⁶ $G(\mathbf{r}_\Omega, \mathbf{r}_0)$ for the problems governed by the Laplace equation (Laplace problems) is given by

$$G(\mathbf{r}_\Omega, \mathbf{r}_0) = \frac{1}{4\pi|\mathbf{r}_\Omega - \mathbf{r}_0|} \quad (9)$$

A simple implementation used here to solve eq 8 numerically divides the boundary into a set of N plane triangular panels indexed by i and j . Fluxes and concentrations within every individual panel Ω_i are set to constants though these values may differ from one panel to another. This breaks the surface integral in eq 8 into a sum of simple integral values over the individual panels. The vectors \mathbf{r}_i and \mathbf{r}_j are the coordinates of the centers of the panels Ω_i and Ω_j . The point \mathbf{r}_0 is moved from the volume to the center points \mathbf{r}_j of the panels Ω_j (Figure 1b, right). This eliminates all volume point concentration in eq 8. Because concentration and flux within a panel are constant, integration needs to be performed only for $G(\mathbf{r}_\Omega, \mathbf{r}_j)$ and $\partial G(\mathbf{r}_\Omega, \mathbf{r}_j)/\partial \mathbf{n}$. The coordinate values for the different panels are distinguished by the index i . Integration is performed for the Green's function over each panel Ω_i , with the coordinate \mathbf{r}_j fixed in the center of panel Ω_j and $\mathbf{r}_{\Omega,i}$ being varied over all possible values within panel Ω_i . The integrals for each panel Ω_i are multiplied with the corresponding flux or concentration value. The products for all panels are summed up. Because the point \mathbf{r}_0 is moved from the volume to the boundary point \mathbf{r}_j , the factor $1/2$ has to be introduced on the left side of eq 8. With the following

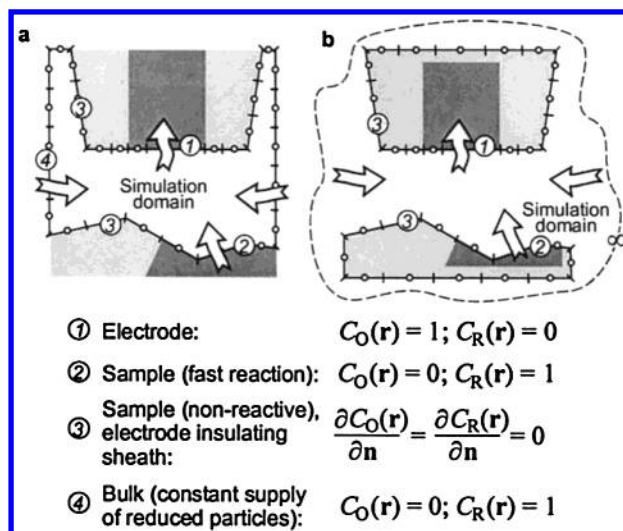


Figure 2. Schematic representation of boundary conditions for SECM simulations with the interior (a) and exterior (b) Laplace formulation. Hollow arrows indicate fluxes.

substitutions

$$C_i = C(\mathbf{r}_i), \mathbf{r}_i \in \Omega_i$$

$$G_{ij} = G(\mathbf{r}_{\Omega,i}, \mathbf{r}_j), \mathbf{r}_{\Omega,i} \in \Omega_i, \mathbf{r}_j \in \Omega_j \quad (10)$$

eq 8 is transformed into the following discrete equation

$$\frac{1}{2} C_j = \sum_{i=1}^N \left(C_i \int_{\Omega_i} \frac{\partial G_{ij}}{\partial \mathbf{n}_i} d\Omega_i - \frac{\partial C_i}{\partial \mathbf{n}_i} \int_{\Omega_i} G_{ij} d\Omega_i \right) \quad (11)$$

The BEM is based on the numerical solution of eq 11 that is used to compose a matrix equation for the unknown boundary values. The composition is performed by moving point \mathbf{r}_j sequentially into the center points of *all* panels Ω_j ($1 \leq j \leq N$) and collecting the matrix values by applying corresponding boundary conditions. The typical boundary conditions for the SECM problems will be given below. As soon as the matrix equation is solved, one obtains complete flux and concentration profiles over the entire boundary. Because the flux profile becomes available, the SECM current can be calculated by integrating the flux values numerically over those N_{el} panels representing the UME surface Ω_{el} :

$$i_T = nFDc_R^* \int_{\Omega_{el}} \frac{\partial C}{\partial \mathbf{n}} d\Omega \approx nFDc_R^* \sum_i \int_{\Omega_{el,i}} \frac{\partial C_i}{\partial \mathbf{n}_i} d\Omega_i = nFDc_R^* \sum_i \left(\frac{\partial C_i}{\partial \mathbf{n}_i} \Omega_i \right) \quad (12)$$

B. Interior vs Exterior Laplace Problem. Implementation of particular geometric and reactive features of a given system is carried out through setting appropriate boundary conditions. The boundary conditions used in all previous simulations with FEM, FDM, and BEM are depicted in Figure 2a. The solid line in Figure 2a indicates schematically the boundaries of the simulation domain. In such a formulation, the task is to solve the *interior* Laplace problem,⁴⁶ i.e., to find a solution *within* a domain limited to particular boundaries. The difficulty with such formulation of SECM problems lays in the correct placement of the bulk boundary in a region where local concentrations do not deviate from the bulk values. In the case of the FDM, using expanding meshes one can set this boundary sufficiently far

from the electrode. However, in case of the BEM, the size of the domain, that can be simulated, is limited, mainly by computing facilities. Moving the bulk boundary apart from the electrode requires setting up additional boundary elements all over the bulk boundary or increasing the size of existing ones. The former leads to an increased size of the matrix and consequently requires much more time and memory resources for calculations. Increasing the size of panels on the other hand increases the computational errors, because fluxes and concentrations are fixed within every panel. It will be shown further that incorrect positioning of the bulk boundary leads to large errors in i_T .

To overcome the problem of the incorrect treatment of the bulk boundary an *exterior* Laplace formulation that completely eliminates the need of the bulk boundary is proposed in this paper. In the exterior formulation, the task is to find a solution *outside* an enclosed domain. The probe and the sample compose a disconnected but enclosed domain, outside which all of the above equations are valid up to the infinity (Figure 2b). This sets the bulk values to an infinite distance from the UME and eliminates the necessity of any a priori assumption on the size of the diffusion layer. Figure 2b also illustrates the definition of the panel set (the mesh) in the exterior formulation. Besides minor changes in system equations, the exterior formulation does not change boundary conditions. The key point in transition from the interior to the exterior formulation is the selection of the redox form of the mediator (R or O) for constructing the matrix equation. It should be the redox form, *whose concentration value at the infinity*, i.e., the bulk concentration, *is zero*. Thus, in our case, assuming an oxidation at the UME, the formulation requires us to solve the matrix equation for C_O . C_R is then found from the mass conservation eq 4. Equations 8 and 11 already assume the exterior formulation and do not require any additional changes, and the same equations for the interior formulation are obtained by multiplying the concentration value on the left part of eqs 8 and 11 by the factor (-1) .

C. Boundary Conditions. The boundary conditions used in this work can be described as follows (see also Figure 2). Assuming diffusion-controlled oxidation of the mediator R, the system behavior can be modeled by the constant maximum concentration of O $C_O(\mathbf{r}_{el}) = 1$ and $C_R(\mathbf{r}_{el}) = 0$ (Dirichlet boundary conditions) at the UME surface:

$$\begin{aligned} C(\mathbf{r}) &= C_O(\mathbf{r}) = 1 \\ C_R(\mathbf{r}) &= 0, \mathbf{r} \in \Omega_{el} \end{aligned} \quad (13)$$

At the insulating and inert parts of the system, including the electrode insulating sheath and insulating (nonreactive) parts of the sample, the boundary conditions do not allow any flux across the boundary. Thus, the flux values on any nonreactive boundary are fixed at zero (Neumann boundary conditions):

$$\frac{\partial C(\mathbf{r})}{\partial n} = \frac{\partial C_O(\mathbf{r})}{\partial n} = \frac{\partial C_R(\mathbf{r})}{\partial n} = 0, \mathbf{r} \in \Omega_{probe,insulator} \text{ or } \mathbf{r} \in \Omega_{sample,insulator} \quad (14)$$

At the reactive parts of the sample with diffusion-controlled reaction rate, species O is immediately reduced back to R thereby restoring the concentration ratio of the undisturbed bulk solution. This leads to the following boundary conditions of

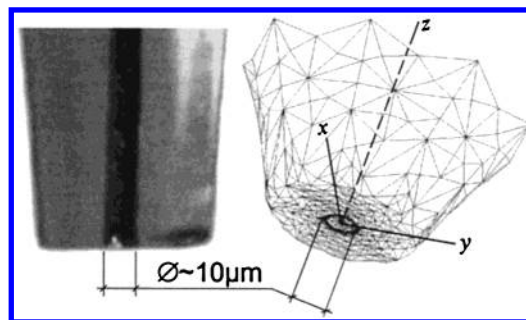


Figure 3. CCD image of a real SECM disc-shaped UME (10 μm diameter, left) and its representation by triangular panels for simulation with the BEM.

the Dirichlet type:

$$\begin{aligned} C(\mathbf{r}) &= C_O(\mathbf{r}) = 0 \\ C_R(\mathbf{r}) &= 1, \mathbf{r} \in \Omega_{sample, conductor} \end{aligned} \quad (15)$$

The case of finite reactivity on the sample is out of the scope of this work and will be provided in one of the following-up works.

Because the system involves the boundary conditions of different types (eqs 13 and 15 versus eq 14), the stability of the matrix system given by eq 11 can be low. To increase the stability and the precision of the calculations, a modification of eq 11 was introduced according to an explanation and guideline given by Kirkup.⁴⁶ Directional derivatives $\partial/\partial \mathbf{n}_j$ along vector \mathbf{n}_j corresponding to the normal of the panel Ω_j were taken for the both sides of eq 11:

$$\frac{1}{2} \frac{\partial C_j}{\partial \mathbf{n}_j} = \sum_{i=1}^N \left(C_i \frac{\partial}{\partial \mathbf{n}_j} \int_{\Omega_i} \frac{\partial G_{ij}}{\partial \mathbf{n}_i} d\Omega_i - \frac{\partial C_i}{\partial \mathbf{n}_i} \frac{\partial}{\partial \mathbf{n}_j} \int_{\Omega_i} G_{ij} d\Omega_i \right) \quad (16)$$

A hybrid equation is obtained by summation of eq 11 with eq 16:

$$\begin{aligned} \frac{1}{2} \left(C_j + \frac{\partial C_j}{\partial \mathbf{n}_j} \right) &= \sum_{i=1}^N C_i \left(\int_{\Omega_i} \frac{\partial G_{ij}}{\partial \mathbf{n}_i} d\Omega_i + \right. \\ &\quad \left. \frac{\partial}{\partial \mathbf{n}_j} \int_{\Omega_i} \frac{\partial G_{ij}}{\partial \mathbf{n}_i} d\Omega_i \right) - \sum_{i=1}^N \frac{\partial C_i}{\partial \mathbf{n}_i} \left(\int_{\Omega_i} G_{ij} d\Omega_i + \right. \\ &\quad \left. \frac{\partial}{\partial \mathbf{n}_j} \int_{\Omega_i} G_{ij} d\Omega_i \right) \end{aligned} \quad (17)$$

The hybrid equation provides a suitable basis for the solution of the exterior Laplace problem for all boundary conditions and is used in our software.

III. Simulation Details

A. Boundary Representation in 3D. The implementation of the BEM requires a simulation domain boundary to be represented as elements with constant fluxes and concentrations within every individual element, i.e., a boundary mesh. A triangular mesh is used in all simulation discussed in this paper. A special routine was developed to construct such meshes for idealized and real electrode and sample geometries. Figure 3 shows the CCD camera image of a real disk electrode together with its triangulation. For convenience, the x - y plane is assumed to be the plane of the sample surface and in an ideal case parallel

to the UME surface. The UME-sample distance d extends along axis z . The mesh is built separately for the electrode and the sample but features the same basic steps. The system geometry is restored from two z height maps, one for the sample and one for the UME. Although this makes it impossible to define geometries that feature complex multilayer structures or panels perpendicular to the x - y plane, such an approach makes it easy to obtain the sample topography directly from STM or AFM images. It also eliminates the necessity of computer-aided design (CAD) software for geometry development and eases the setup of the simulation boundary and mesh adaptation.

The mesh is built up in several steps. First, the topography image is covered with the trivial axisymmetric mesh given in the form of a spider web. The center of this initial mesh is set to the geometric center of the UME. For the sample, the center has the same (x, y) coordinates as the center of the UME mesh. Consequently, if the electrode is moved within a line scan, the sample mesh will be automatically reconstructed even if the UME mesh stays unchanged. The initial mesh defines also how large the simulation area is. Usually the radius of the initial mesh for the sample is selected to be approximately 15 times larger than the effective UME radius, whose definition is given below, assuming a negligible influence of the sample features beyond this distance on the UME current. Setting the initial mesh in the form of a spider web creates an expanding mesh with the most developed part in the center of the UME. The following steps include a mesh refinement. Especially small panels have to be used in the areas where boundary conditions of different types meet (i.e., at the reactive/nonreactive border). The refinement of the mesh at the reactive/nonreactive border provides a better developed mesh in regions where significant concentration gradients and larger fluxes could be found (Figure 3, see also Figure 8). The possibility of automatic mesh refinement based on the evaluation of concentration and flux gradients from the previous solution in an iterative procedure was also implemented. It has not been carefully tested yet, because it requires extensive computational resources and time. The calculations presented here have been made without involving automatic mesh refinement.

B. Software. The simulations have been performed with an in-house-developed software. It is based on the solution of the matrix equation given by eq 17. The system uses a triangular boundary mesh representation. The matrix assembly involves numerical surface integration of Green's function (eq 17) that is performed by Gauss-Legendre quadrature rules.⁴⁸ The BEM generates a fully populated matrix that is solved by the low-up (LU) decomposition method.⁴⁹ Depending on the extent of the mesh development, the simulations carried out on a 1.7 GHz personnel computer (PC) took from 1 min (for 1200 mesh elements) to 20 min (for 2800 mesh elements) per i_T value, i.e., per single geometric arrangement of UME and sample. Additional information on the software can be found in ref 50.

IV. Results and Discussion

A. Method Verification. Fulian et al.⁴²⁻⁴⁴ have proven the fundamental applicability of the BEM with the interior Laplace formulation for the purposes of SECM simulations. Here the improved performance of the BEM with the exterior Laplace formulation is demonstrated for handling SECM tasks.

1. Simulation Precision with the Interior vs Exterior Formulation of the Laplace Problem. The correct SECM setup assumes the bulk solution to be appreciably larger than the extension of the diffusion layer of the UME probe. This ensures sufficient mediator supply to the electrode vicinity and thus a

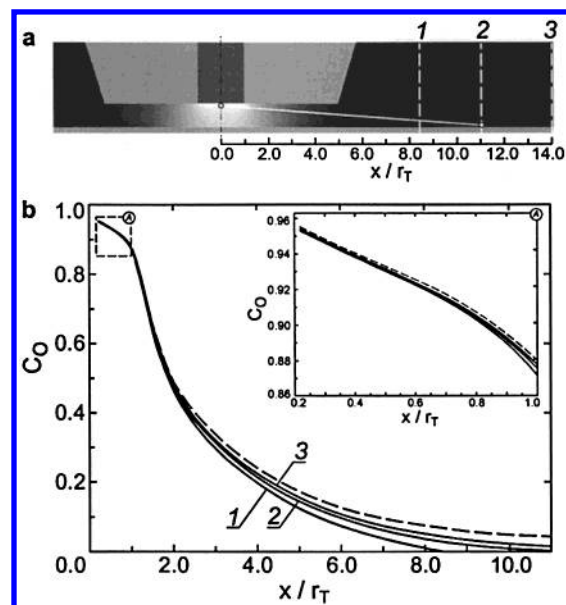


Figure 4. Comparison of interior and exterior formulation of the Laplace problem. (a) Setup of the simulation domain around a disk-shaped UME, $RG = 5.1$, insulating, nonreactive, plane sample parallel to the UME, $L = 1.2$. The bulk boundary for the interior formulation had almost a cylindrical shape coaxial with the UME and different radii of $14 r_T$ (1), $11.2 r_T$ (2), and $8.4 r_T$ (3). (b) Calculated normalized concentration for the interior formulation (solid lines 1–3) and exterior formulation (dashed line) along the white line in Figure 4a. The inset shows the concentration profiles in the vicinity of the electrode.

steady-state bulk signal. This, in turn, requires an accurate definition of the bulk boundary for the numerical simulations. It must be prevented that the diffusion front reaches the simulation boundaries. As mentioned above, simulations with FDM overcome this problem by using expanded meshes, thereby moving the boundary of the bulk far from the electrode. In contrast, setting the bulk far from the electrode causes accumulating numerical errors for the BEM simulations with *interior* formulation either because of large surface elements or a large number of those. Exterior formulation eliminates the problem because it does not involve any bulk boundary and solves the problem up to the infinity. To examine the dependence of the results on the selection of the simulation boundary when using the interior formulation, the situation of disc-shaped UMEs above a plane insulator in parallel orientation was simulated using the interior formulation with different simulation domains (Figure 4a, 1–3) and with the exterior formulation. In addition to the calculation explained above, the concentrations for all volume points were calculated using eq 8 with the flux and concentration values at the boundary obtained from eq 17. For the insulating, nonreactive sample, the diffusion front spreads relatively far from the electrode. The result is therefore greatly affected by the positioning of the bulk boundary. In the interior, BEM formulation the position of the boundary of the solution bulk corresponds to a surface where the particles converted at the UME are regenerated. It is therefore intuitively clear that the position of this surface must have a rather strong influence.

The concentration profiles in Figure 4b, solid lines 1–3 illustrate the critical importance of the boundary selection when using the interior formulation. For comparison, the result using the exterior formulation is given as dashed line in Figure 4b. On small distances from the electrode, one cannot see a very large discrepancy in the concentration profiles (inset of Figure 4b), but because of the integration over the electrode area, it

TABLE 1: Relative Errors in the SECM Current Calculated Using Interior and Exterior Formulation as Compared to the Values Obtained with FDM in Ref 38^a

| configuration in Figure 4 | radius of the simulation domain | relative error [%] |
|---------------------------|---------------------------------|--------------------|
| 1 | 8.4 r_T | 9.86 |
| 2 | 11.2 r_T | 6.20 |
| 3 | 14.0 r_T | 4.51 |
| exterior BEM | does not apply | 0.405 |

^a See Figure 4 for details on the simulation domains.

introduces a major error in the electrode current (Table 1). Furthermore, if a concentration value at a point distant from the electrode is to be found, its error will be determined by the differences in the right-hand tails of the curves in Figure 4b, which have essential distinctions. It becomes clear that it is not sufficient to increase the simulation boundary in order to improve the accuracy of the results. As shown in Table 1, the relative deviation of the i_T obtained from the interior formulation can be as high as 10%. This is in agreement with the precision of the first BEM calculations for SECM in ref 43. In Figure 14 of ref 43, a line scan for a disk UME with $RG = 10$ and $L = 1$ is calculated extended from a plane conductive region with diffusion-controlled positive feedback to an inert insulator. Far away from the transition region, the normalized currents $i_T(L = 1)$ are 0.582 and 1.306 for the insulator and conductor, respectively. These values should be equal to the values obtained above infinitely large uniform samples. For a very similar setup ($RG = 10.2$, $L = 1$), the analytical approximations in ref 38 give $i_T(L = 1)$ values of 0.485 for the insulator and 1.556 for the conductor. The deviation between the results of the two simulation strategies is in the same order of magnitude, if not larger, than between our attempts with the interior formulation and the FDM data of ref 38. Therefore, the deviations are likely due to the unavoidable errors of the interior BEM formulation if applied to SECM problems. In contrast, the results of the exterior formulation are in quantitative agreement with FDM simulation of Amphlett and Denuault³⁸ (Table 1 and below).

2. Simulation Precision in Comparison to FDM Simulation for Semiinfinite Times. Direct verification of the BEM stability and convergence is a very difficult mathematical task. Thus, the method is verified by a comparison of its simulation results with results obtained earlier by FDM simulation techniques. For testing purposes, two axial symmetric geometries have been selected, i.e., the microdisk and the hemispherical electrodes with their symmetry axes oriented perpendicular to a perfectly plane sample. The microdisk electrode is the most frequently treated problem for which both several simulation as well as a very precise experimental data are available. The case of the hemisphere has been simulated and required a considerable effort for coordinate transformation. Experimental data are not of the same precision as for the microdisk because of problems preparing hemispherical microelectrodes with exact definition of their geometry. It will be shown that the BEM treatment simplifies the calculation without compromising precision. Both cases have been processed in 2D in the original papers of Amphlett and Denuault³⁸ and Selzer and Mandler³⁹ because of the axial symmetry. Both groups used the alternate direction FDM considering also transient behavior. Despite the possibility of reduction to a 2D problem, the steady-state situation of the pure 3D tasks was simulated in this paper to check the accuracy of the adapted simulation method. Comparison was made to the results of refs 38 and 39 for semiinfinite time.

Figure 5, curves 1–3, represents the simulation results for the normalized microdisk approach curves. For testing purposes,

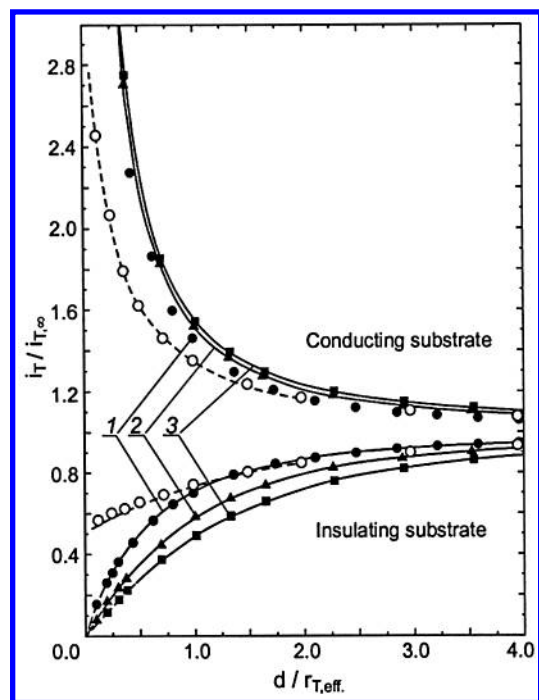


Figure 5. Normalized approach curves for disk-shaped UME (curves 1–3) and hemispherical UME (curve 4) to a plane sample (insulating nonreactive sample or diffusion controlled positive feedback over a conductor) oriented perpendicular to the symmetry axis of the UME calculated with the BEM for the following UME: microdisks, $RG = 2.0$ (●), 5.1 (▲), 10.2 (■), and hemisphere, $RG = 10.0$ (○). For comparison, analytical approximations of the FDM results are given as solid lines for disks with RG values of 2.0 (insulator only, curve 1),³⁸ 5.1 (curves 2),³⁸ and 10.2 (curves 3)³⁸ and hemisphere with $RG = 10$ (dashed line, curve 4)³⁹ renormalized in accordance to eq 19. The fitting curves are plotted as dashed lines for the region where their errors may exceed 1%.

the RG values were selected equal to those for which Amphlett and Denuault³⁸ have found analytical approximations for their simulation results within 1% error bars. This allowed a direct comparison of our results with those obtained by an entirely different simulation approach (Figure 5). Within the whole range of L values, the data obtained with the BEM for pure steady-state situation are in a very good agreement with those obtained by the simulations of transient eq 5 assuming time approaches infinity. For the positive feedback, very small L values could be simulated because the diffusion layer of the UME is confined to the vicinity of the electrode because of the regeneration of the mediator at the sample. In case of the negative feedback, a fine mesh is required up to large distances from the UME because the diffusion front extends beyond the UME-sample gap. This increases the simulation time significantly and makes simulation of such cases challenging. This is, however, a feature shared with the FDM simulation strategies.

The comparison against FDM simulations of the time-dependent behavior of hemispherical microelectrodes by Selzer and Mandler,³⁹ Figure 5, curve 4, for electrodes having the same RG value of 10 are defined in the same manner as for the microdisk electrode. The simple geometry variation from microdisk to hemisphere requires an extensive mathematical pretreatment in the FDM that involves coordinate transformations. The BEM handles this particular and other more complicated geometries without any additional mathematical pretreatment. To allow a direct comparison of the dataset with that of ref 39, the probe–sample distance normalization was made here to the effective radius $r_{T,eff}$ defined as the radius of a disk that has the same area as the area of the considered probe

electrode Ω_{el} :

$$r_{T,eff} = \sqrt{\frac{\Omega_{el}}{\pi}} \quad (18)$$

The conceptual advantage of this normalization is its more general applicability. For instance, nanometer-sized probe electrodes often feature no axial symmetry, and so, no radius is defined for normalizing d . Moreover, such normalization has also a methodic advantage because the current is derived through surface integration over the electrode area Ω_{el} . Hence, it depends more on the area than on spatial dimensions, though this dependence is not linear. For the hemisphere, the electrode area can be directly calculated through the radius of the hemisphere $r_{hemisphere}$

$$r_{T,eff} = \sqrt{2}r_{hemisphere} \quad (19)$$

In Figure 5, curve 4, the dashed lines represent the values of Selzer and Mandler³⁹ renormalized in accordance to eq 19. The BEM simulations agree very well with the FDM simulations in the whole range of L values. The only deviations one can see are for the insulating sample at small L . They originate from the requirement of increased mesh sizes to maintain the same level of precision easily obtained for large L values (see discussion on microdisks above). The crossing of the lines for the hemisphere ($RG = 10$) and the microdisk with $RG = 2$ approaching an insulator is expected because at large distances the hemisphere is not very different from the equivalent microdisk while close to the surface all microdisk currents will tend toward zero in contrast to the hemisphere.

B. Problems with no Axial Symmetry: Tilted Microdisk Electrode. Correct electrode alignment, i.e., placing the electrode z axis (Figure 3) perpendicular to the sample plane, is a challenging experimental problem. An interesting question is to which extent currents $i_T(d, \alpha)$ deviate at an UME tilted by an angle α off the normal of the sample surface from the values $i_T(d, \alpha = 0)$. Such a problem has not been addressed yet by FDM because of the lack of axial symmetry. A family of SECM approach curves for a disk-shaped UME with different tilt angle α was calculated with the exterior BEM (Figure 6). The RG value of the electrode was set to 5.1, and the tilt angle assumed values from 1° to 8° . The system geometry is schematically depicted in Figure 6a. Figure 6b displays the data counting d between the sample and the center of the UME. Because of the very similar probe geometry, the approach curves for different α are hardly distinguishable. The tilt does not much affect the geometry of the whole system on large L , and the only noticeable deviations occur at small probe-sample distances $L < 1$. At larger distances, the family of approach curves almost superimpose. However, if the distance is counted off the probe part closest to the sample, i.e., from the glass edge in this case, the approach curves behave remarkably different. Such a distance measurement is for example effective within the shear-force distance control mechanism,^{19,23,24} where the shear-force signal depends on the shortest distance between the probe and the sample and not on the distance counted off the active part of the UME. Figure 6c gives the approach curves with the probe-sample distance d_{glass} measured between the sample and the closest point of the insulating sheath. With increasing tilt, the electrode seems to behave less sensitive (less effective blocking of diffusion and less effective positive feedback). If the geometry of the UME is known, the simulated approach curves with the distance plotted as d_{glass} (Figure 6c) can be used in conjunction with experimental probe-sample distance values d_{glass} obtained

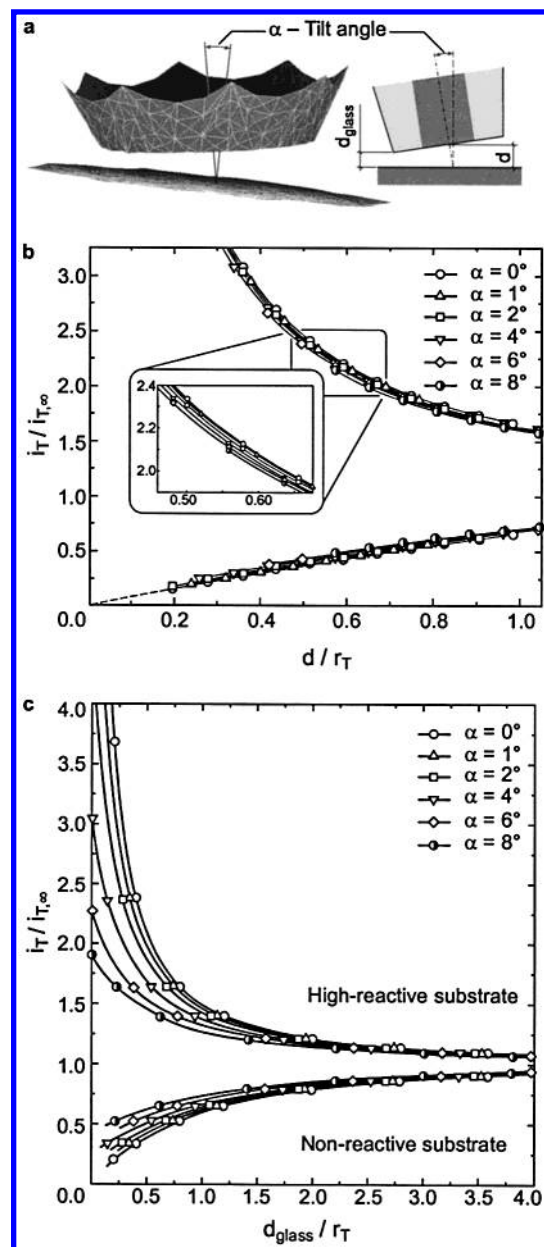


Figure 6. Calculated SECM approach curves for tilted microdisk electrode ($RG = 5.1$) in dependence on the tilt angle α . (a) geometric configuration and notations; (b) approach curves with d counted off the UME center; (c) approach curves with d_{glass} counted as the smallest distance between the sample and the insulating sheath.

for instance from shear-force data to provide a correct electrode alignment because the SECM current itself (plotted from the electrode center) is almost not affected by the tilt (Figure 6b).

C. Spatial Resolution of SECM Images. The resolution of the SECM is the ability to distinguish two closely spaced objects distinguished by its topography or reactivity from the surrounding matrix. Because of the diffusion control over the SECM current, resolution is affected by the probe geometry and the setup parameters like the probe-sample distance. The probe-sample distance affects the resolution in two ways. Because of the extension of the diffusion layer as the distance increases, the current is affected by the sample features situated farther from the UME, thus leading to the decrease of the resolution. This is especially important in the imaging of low-reactive features in a highly reactive matrix. Second, the maximum sensitivity of the SECM, given by the difference between approach curves for positive and negative feedback modes,

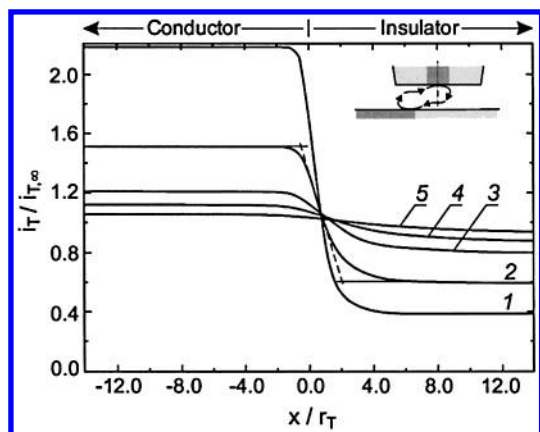


Figure 7. SECM line scans simulated with the BEM exterior formulation for a disk-shaped UME ($RG = 5.1$) over the border of a conducting surface (diffusion-controlled positive feedback) toward an inert insulating surface for different normalized probe sample distances L of 0.5 (1), 1.0 (2), 3.0 (3), 3.0 (4), and 5.0 (5).

decreases with increasing distance. This is equivalent to a decrease in sensitivity (for instance, the signal difference for hindered diffusion and diffusion-controlled positive feedback). With increasing distance, it becomes more and more difficult to distinguish a signal from the noise.

The BEM enables simulations of the SECM line scans as well as images. In Figure 7, simulated line scans are given for different d , aiming to analyze the resolution of standard microdisk electrodes. Despite the fact that the UME in this case is a microdisk and thus axisymmetric, its line scans can be calculated with other techniques only with many difficulties because the absence of axial symmetry for the sample brakes the symmetry of the system as a whole. For all calculated curves, the current tails over conducting and insulating regions. This is evident from a comparison of the line scan with the dashed line over the insulator (Figure 7, curve 2), where the tails are not symmetrical. Even if the UME is located above the insulator but with the sheath still over the conductor, a fraction of the mediator will be regenerated at the conductor (Figure 7, inset). This leads to the drawn-out tail of the curves over the insulator. If the UME is placed over the conductor, a mediator regeneration at the sample occurs only underneath the UME, and the insulating regions do not have any influence on i_T . Therefore, d must be kept small when imaging low-reactive features positioned within a highly reactive matrix.

The effect of the overall probe geometry on the resolution and sensitivity can be analyzed in the following numerical experiment. The line scans for several microdisk electrodes with different RG values are simulated over conducting bands positioned in a plane insulating matrix. This problem was posed by Amphlett and Denuault³⁸ where the simulations were made in 2D assuming an infinitely long band electrode scanning over two parallel infinitely long bands on the sample (in order to maintain a 2D system). Because of the deviation in the probe geometry, the results are purely qualitative. Now this problem can be treated in 3D involving standard microdisk UME. The system geometry and the mesh used in simulations are shown in Figure 8a (a microdisk UME, $RG = 5.1$). It is also seen how the mesh is refined in the areas close to the separation of reactive regions and close to the center of the UME, where most of fluxes are expected (view from beneath the sample). The mesh used in these simulations features about 2500 panels and requires approximately 20 min to obtain a single point of a line scan. The calculated line scans for electrodes with RG values of 2.0, 5.1, and 10.2 are given in Figure 8b. The signal calculated for

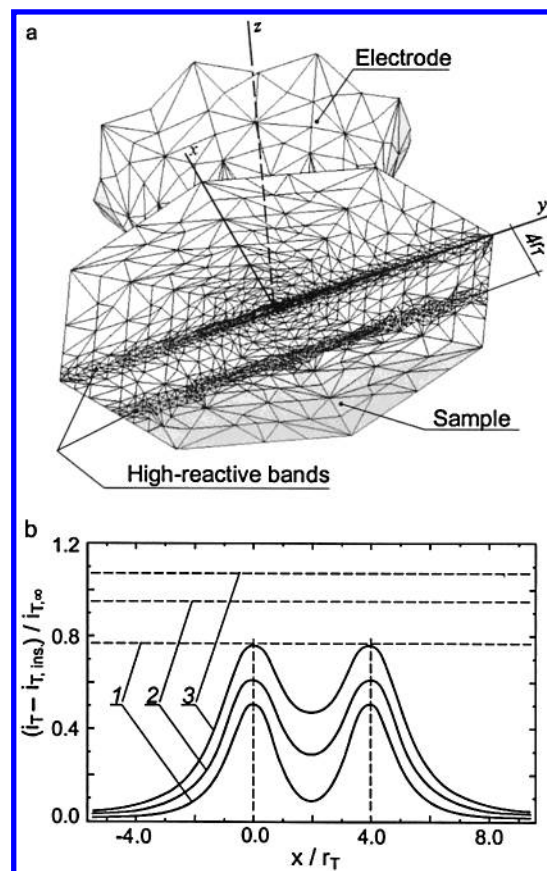


Figure 8. Simulated line scans of microdisk electrodes scanning over an inert insulating sample with two embedded conductive bands. (a) Geometry of the system and the mesh used for BEM simulation with exterior formulation. (b) Simulation results for UME probes with RG values of 2.0 (curve 1), 5.1 (curve 2), and 10.2 (curve 3) at $d = r_T$. The sample is a plane parallel-oriented inert insulator with two embedded conducting bands causing diffusion-controlled mediator regeneration. Bandwidth, $0.5 r_T$; midpoint-to-midpoint distance of the bands, $4 r_T$. The dashed horizontal lines indicate $i_T(d)$ for the diffusion-controlled positive feedback above an infinite large conducting region giving the maximum possible values of i_T for every particular electrode at $d = r_T$.

every particular electrode situated at $d = r_T$ above an insulating inert sample was subtracted for all curves. The dashed lines represent the maximum possible $i_T(d)$ over an infinite large conductor with diffusion-controlled positive feedback. It is seen that at larger RG values the sensitivity of the SECM is better; that is, the signal difference conductor–insulator is large. However, the resolution is better for smaller RG values; for instance, the valley between the peaks is better developed in the corresponding line scans. The results of our calculations confirm the qualitative results of Amphlett and Denuault³⁸ but have quantitatively correct values in each data point.

D. SECM in Shear-Force Distance Control Mode. The merit of the SECM as a scanning technique is in the possibility to image distributions of heterogeneous reaction rates of surfaces. Though it can also be used to map the sample topography, this is not considered to be the strength of SECM because its topographical resolution is much lower than that routinely achieved by ECSTM or SFM measurements. On the other hand, reaction rate images are always convoluted with topographic information except for very smooth interfaces such as liquid–liquid interfaces. To reduce the influence of topographic features on reaction rate images, current-independent distance control systems are used as mentioned in the Introduction.^{23–32} It is often assumed that the effect of topo-

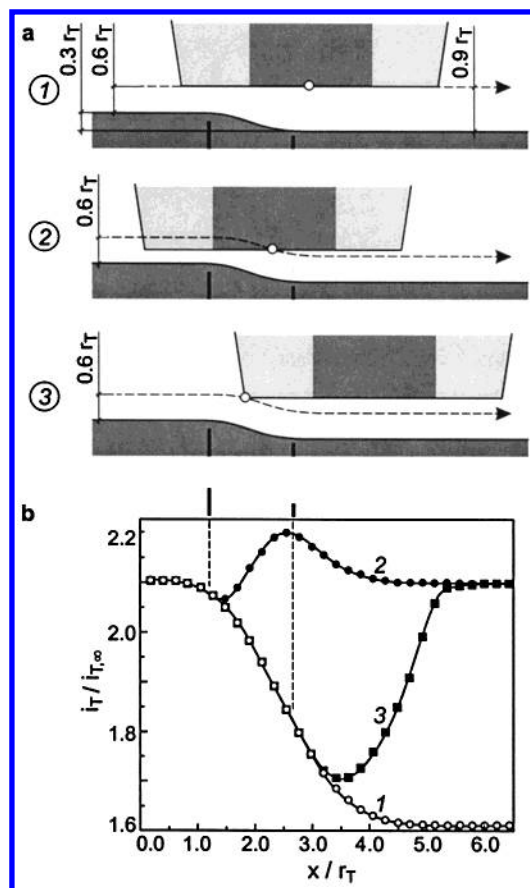


Figure 9. Line scan simulations of the SECM operating in different distance control modes. (a) Schematics of the UME path with correct proportions in the constant height mode (1), the constant distance mode (2), and a shear-force controlled constant distance mode (3). (b) Simulation results using the BEM with exterior formulation for the constant height mode (\square), the constant distance mode (\bullet), and a shear-force controlled constant distance mode (\blacksquare). $RG = 5.1$. Vertical marks on the schematic geometries correspond to the marked spatial coordinates in part b.

graphical features could be eliminated when working with a constant d . However, because of the finite dimension of the UME, a complete elimination of topographic effects is impossible. BEM simulations of line scans above a conductive surface with a topographic step allows us to evaluate the effect of different distance regulation regimes. Three cases are considered: First, the result of the so-called constant height mode is given in Figure 9a, case 1, when the UME is scanned in a fixed plane parallel to the larger part of the sample surface. Figure 9a, case 2 shows a “true” constant distance mode, when the distance from the center of the active electrode area is maintained at a constant distance to the sample. Figure 9a, case 3 shows the constant distance mode as performed by a shear-force control system. The main distinctive feature of the shear-force distance control is that the distance d_{glass} is counted off any point of the probe body (electrode plus sheath) currently being closest to the sample (see distinctions in the electrode positioning in Figure 9a, cases 2 and 3).

The results of the BEM line scan simulations for all three cases are given in Figure 9b. The line scans were performed with a disk-shaped UME of $RG = 5.1$ over a conductive sample causing diffusion-controlled positive feedback and featuring a topographic step between $x/r_T = 1.2$ and $x/r_T = 2.6$ as shown in Figure 9a. The normalized current changes from 2.1 to 1.62 in the constant height mode (no distance control system active) when scanning over the step edge. As expected, the distance

control mechanisms (cases 2 and 3) can partially eliminate the topographic influence on i_T . This is evident from the fact that a constant i_T is obtained for the plane regions of the surface far away from any step edge (Figure 9b, curve 2 and 3, $x/r_T < 0.6$, $x/r_T > 5$). However, close to the step edge itself, the current deviates by up to 10% from the values over the plane parts of the surface even with distance control mechanisms! Although the deviations of the current in cases 2 and 3 are spatially confined to the vicinity of topographic features and limited to 10% of i_T , none of these two constant distance modes eliminates the topographical effect. The effect was also seen experimentally in the measurements using a combined ECSTM–SECM instrument.³² The results will be published in a subsequent paper.

From Figure 9a, it becomes clear that the size of the region around a step edge where the influence of the topographic feature cannot be eliminated is different for the different distance control modes. In Figure 9a, case 2, where a constant d is maintained between the UME and the sample, the disturbed region has an extension roughly equivalent to the UME diameter (in Figure 9b, curve 2). The RG value has an influence mainly on the achievable resolution and the sensitivity of the probe as shown in Figure 8. In the case of a shear-force distance control (in Figure 9b, curve 3), one has to expect a region disturbed by topographical influences with a size approximately equivalent to the diameter of the entire probe (UME plus sheath).

V. Conclusions

Steady-state amperometric SECM responses were simulated in three-dimensions with the boundary element method. The problem was formulated in the exterior Laplace formulation in contrast to the interior Laplace formulation used previously by Fulian et al.^{42–44} for the BEM simulations in SECM. The new formulation allowed us to decrease the computational errors arising from the incorrect positioning of the bulk boundary in the interior formulation. To further improve the precision and the liability of the calculation, expanding meshes have been used to cover larger simulation domains. The meshes are specifically adapted to provide fine meshes around topographic features and where the reactivity of the probe and the sample changes. In the same manner as in the simulations with the FDM, the expanding meshes cover much larger areas and thus allow us to consider the sample and electrode features on larger distances from the electrode without causing significant additional numerical errors. The applicability of the method with exterior formulation and expanding meshes was verified by series of simulations for approach curves of microdisk and hemispherical UMEs to flat samples that had been treated previously with the two-dimensional FDM.^{38,39} The results of the BEM simulation were in excellent agreement with the FDM simulation of the same geometries. Significant deviations of around 10% occurred when treating the problems with BEM and interior formulation.

The ability of BEM simulations to address nonsymmetric steady-state problems was used to analyze the influence of UME tilt on approach curves. Furthermore, the influence of d , RG , and r_T on SECM resolution was tested in different setups. Finally, the analysis of different distance control modes of the SECM has been made by simulating the SECM line scans over the samples of uniform reactivity featuring a topographic step edge. The constant distance mode including that used in shear-force distance control showed a reduction of the topographical effect on i_T . However, because of the finite size of the probe, the topographical effect cannot be eliminated in the vicinity of the step edge. The disturbance may be as high as 10% of i_T .

Acknowledgment. This project is carried out within the focus program SPP 1030 "Foundation of Electrochemical Nanotechnology" (Wi 1617/2-5) of the Deutsche Forschungsgemeinschaft. O.S. also acknowledges the Graduate Course GK 152 "Physical Chemistry of Surfaces and interfaces" at the Wilhelm Ostwald Institute for Physical and Theoretical Chemistry at the University of Leipzig as well as the German Academic Exchange Office (DAAD) for the financial support.

References and Notes

- (1) Bard, A. J.; Fan, F.-R.; Mirkin, M. V. In *Electroanalytical Chemistry, A Series of Advances*; Bard, A. J., Ed.; Marcel Dekker: New York, 1994; Vol. 18, p 243.
- (2) *Scanning Electrochemical Microscopy*; Bard, A. J., Mirkin, M. V., Eds.; Marcel Dekker: New York, 2001.
- (3) Engstrom, R. C.; Pharr, C. M. *Anal. Chem.* **1989**, *61*, A1099.
- (4) Bard, A. J.; Fan, F.-R. F.; Pierce, D. T.; Unwin, P. R.; Wipf, D. O.; Zhou, F. *Science* **1991**, *254*, 68.
- (5) Unwin, P. R.; Macpherson, J. V. *Chem. Soc. Rev.* **1995**, *24*, 109.
- (6) Mirkin, M. V. *Anal. Chem.* **1996**, *68*, A117.
- (7) Mandler, D.; Meltzer, S.; Shohat, I. *Isr. J. Chem.* **1996**, *36*, 73.
- (8) Unwin, P. R. *J. Chem. Soc., Faraday Trans.* **1998**, *94*, 3138.
- (9) Barker, A. L.; Gonsalves, M.; Macpherson, J. V.; Slevin, C. J.; Unwin, P. R. *Anal. Chim. Acta* **1999**, *385*, 223.
- (10) Basame, S. B.; White, H. S.; *J. Phys. Chem. B* **1998**, *102*, 9812.
- (11) Wittstock, G.; Schuhmann, W. *Anal. Chem.* **1997**, *69*, 5059.
- (12) Shiku, H.; Matsue, T. In *Sensors Update*; Baltes, H., Göpel, W., Hesse, J., Eds.; Wiley-VCH: Weinheim, Germany, 2000; Vol. 6, p 231.
- (13) Wijayawardhana, A.; Wittstock, G.; Halsall, H. B.; Heineman, W. R. *Anal. Chem.* **2000**, *72*, 333.
- (14) Mirkin, M. V.; Horrocks, B. R. *Anal. Chim. Acta* **2000**, *406*, 119.
- (15) Wittstock, G. *Fresenius J. Anal. Chem.* **2001**, *370*, 303.
- (16) The use of potentiometric probes in SECM is documented as well but requires a different approach for simulation, which is not considered further in this paper. For examples, see: Horrocks, B. R.; Mirkin, M. V.; Pierce, D. T.; Bard, A. J. Nagy, G.; Toth, K. *Anal. Chem.* **1993**, *65*, 1213. Nagy, G.; Nagy, L. *Fresenius J. Anal. Chem.* **2000**, *366*, 735.
- (17) Wipf, D. O.; Bard, A. J.; Tallman, D. E. *Anal. Chem.* **1993**, *65*, 1373.
- (18) Borgwarth, K.; Ebling, D. G.; Heinze, J. Ber. *Bunsen-Ges. Phys. Chem.* **1994**, *98*, 1317.
- (19) Ludwig, M.; Kranz, C.; Schuhmann, W.; Gaub, H. E. *Rev. Sci. Instrum.* **1995**, *66*, 2857.
- (20) Wittstock, G.; Emons, H.; Kummer, M.; Kirchhoff, J. R.; Heineman, W. R. *Fresenius J. Anal. Chem.* **1994**, *348*, 712.
- (21) Shao, Y.; Mirkin, M. V.; Fish, G.; Kokotov, S.; Palanker, D.; Lewis, A. *Anal. Chem.* **1997**, *69*, 1627.
- (22) Williams, D. E.; Mohiuddin, T. F.; Zhu, Y. Y. *J. Electrochem. Soc.* **1998**, *145*, 2664.
- (23) Hengstenberg, A.; Kranz, C.; Schuhmann, W. *Chem. Eur. J.* **2000**, *6*, 1547.
- (24) James, P.; Garfias-Mesias, L. F.; Moyer, P. J.; Smyrl, W. H. *J. Electrochem. Soc.* **1998**, *4*, 64.
- (25) Alpulche-Aviles, M. A.; Wipf, D. O. *Anal. Chem.* **2001**, *73*, 4873.
- (26) Jones, C. E.; Macpherson, J. V.; Barber, Z. H.; Somekh, R. E.; Unwin, P. R. *Electrochem. Commun.* **1999**, *1*, 55.
- (27) Jones, C. E.; Macpherson, J. V.; Unwin, P. R. *J. Phys. Chem. B* **2000**, *104*, 2351.
- (28) Macpherson, J. V.; Unwin, P. R. *Anal. Chem.* **2000**, *72*, 276.
- (29) Macpherson, J. V.; Unwin, P. R. *Anal. Chem.* **2001**, *73*, 550.
- (30) Kranz, C.; Friedbacher, G.; Mizaikoff, B.; Lugstein, A.; Smoliner, J.; Bertagnolli, E. *Anal. Chem.* **2001**, *11*, 2491.
- (31) Kucernak, A. P.; Chowdhury, P. B.; Wilde, C. P.; Kelsal, G. H.; Zhu, Y. Y.; Williams, D. E. *Electrochim. Acta* **2000**, *45*, 4483.
- (32) Treutler, T. H.; Wittstock, G. In *Proceedings of 2nd International Workshop on Scanning Electrochemical Microscopy*; Denuault, G., Ed.; The University of Southampton: Southampton, U.K., 2001; p 23.
- (33) Mirkin, M. V.; Fan, F.-R. F.; Bard, A. J. *J. Electroanal. Chem.* **1992**, *328*, 47.
- (34) Kwak, J.; Bard, A. J. *Anal. Chem.* **1989**, *61*, 1221.
- (35) Unwin, P. R.; Bard, A. J. *J. Phys. Chem.* **1991**, *95*, 7814.
- (36) Zhou, F.; Unwin, P. R.; Bard, A. J. *J. Phys. Chem.* **1992**, *96*, 4917.
- (37) Bard, A. J.; Mirkin, M. V.; Unwin, P. R.; Wipf, D. O. *J. Phys. Chem.* **1992**, *96*, 1861.
- (38) Amphlett, J. L.; Denuault, G. *J. Phys. Chem. B* **1998**, *102*, 9946.
- (39) Selzer, Y.; Mandler, D. *Anal. Chem.* **2000**, *72*, 2383.
- (40) Lee, Y.; Amemiya, S.; Bard, A. J. *Anal. Chem.* **2001**, *73*, 2261.
- (41) Galceran, J.; Cecilia, J.; Companys, E.; Salvador, J.; Puy, J. *J. Phys. Chem. B* **2000**, *104*, 7993.
- (42) Fulian, Q.; Fisher, A. C. *J. Phys. Chem. B* **1998**, *102*, 9647.
- (43) Fulian, Q.; Fisher, A. C.; Denuault, G. *J. Phys. Chem. B* **1999**, *103*, 4387.
- (44) Fulian, Q.; Fisher, A. C.; Denuault, G. *J. Phys. Chem. B* **1999**, *103*, 4393.
- (45) Brebbia, C. A.; Dominguez, J. *Boundary Elements: An introductory course*; Computational Mechanics Publications: Southampton: U.K., 1994.
- (46) Kirkup, S. *The BEM for Laplace Problems*; ISS: www.boundary-element-method.co.uk/bemlap/manual.htm
- (47) Frayce, D.; Khayat, R. E.; Derdouri, A. *Numer. Heat. Transfer, Part A* **1996**, *29*, 243.
- (48) Laursen, M. E.; Gellert, M. *Int. J. Numer. Methods Eng.* **1978**, *12*, 67.
- (49) Press, W. H.; Teukolsky, S. A.; Vetterling, W. T.; Flannery, B. P. *Numerical Recipes in C: The Art of Scientific Computing*; 2nd ed.; Cambridge University Press: New York, 1993.
- (50) Details to the software are given on the Internet at <http://www.chemie.uni-oldenburg.de/pc/wittstock/>